Gemini Near Infrared Spectrograph–Distant Quasar Survey: Prescriptions for Calibrating UV-based Estimates of Supermassive Black Hole Masses in High-redshift Quasars

Cooper Dix[1] , Brandon Matthews[1] , Ohad Shemmer[1] , Michael S. Brotherton[2] , Adam D. Myers[2], I. Andruchow[3,4],
W. N. Brandt[5,6,7] , Gabriel A. Ferrero[8,9], Richard Green[10] , Paulina Lira[11] , Richard M. Plotkin[12,13] ,
Gordon T. Richards[14] , and Donald P. Schneider[5,6]

[1] Department of Physics, University of North Texas, Denton, TX, 76203, USA; cooperdix@my.unt.edu
[2] Department of Physics and Astronomy, University of Wyoming, Laramie, WY, 82071, USA
[3] Facultad de Ciencias Astronómicas y Geosicas, Universidad Nacional de La Plata, Paseo del Bosque, B1900FWA, La Plata, Argentina
[4] Instituto Argentino de Radioastronomía, CONICET-CICPBA-UNLP, CC5 (1897) Villa Elisa, Prov. de Buenos Aires, Argentina
[5] Department of Astronomy and Astrophysics, The Pennsylvania State University, University Park, PA 16802, USA
[6] Institute for Gravitation and the Cosmos, The Pennsylvania State University, University Park, PA 16802, USA
[7] Department of Physics, 104 Davey Lab, The Pennsylvania State University, University Park, PA 16802, USA
[8] Facultad de Ciencias Astronómicas y Geofísicas, Universidad Nacional de La Plata, Paseo del Bosque, B1900FWA La Plata, Argentina
[9] Instituto de Astrofísica de La Plata, CONICET-UNLP, CCT La Plata, Paseo del Bosque, B1900FWA La Plata, Argentina
[10] Steward Observatory, University of Arizona, 933 N Cherry Avenue, Tucson, AZ 85721, USA
[11] Departmento de Astronomía, Universidad de Chile, Casilla 36D, Santiago, Chile
[12] Department of Physics, University of Nevada, Reno, NV 89557, USA
[13] Nevada Center for Astrophysics, University of Nevada, Las Vegas, NV 89154, USA
[14] Department of Physics, Drexel University, 32 S. 32nd Street, Philadelphia, PA 19104, USA

Abstract

The most reliable single-epoch supermassive black hole mass (M_{BH}) estimates in quasars are obtained by using the velocity widths of low-ionization emission lines, typically the Hβ λ4861 line. Unfortunately, this line is redshifted out of the optical band at $z \approx 1$, leaving M_{BH} estimates to rely on proxy rest-frame ultraviolet (UV) emission lines, such as C IV λ1549 or Mg II λ2800, which contain intrinsic challenges when measuring, resulting in uncertain M_{BH} estimates. In this work, we aim at correcting M_{BH} estimates derived from the C IV and Mg II emission lines based on estimates derived from the Hβ emission line. We find that employing the equivalent width of C IV in deriving M_{BH} estimates based on Mg II and C IV provides values that are closest to those obtained from Hβ. We also provide prescriptions to estimate M_{BH} values when only C IV, only Mg II, and both C IV and Mg II are measurable. We find that utilizing both emission lines, where available, reduces the scatter of UV-based M_{BH} estimates by $\sim$15% when compared to previous studies. Lastly, we discuss the potential of our prescriptions to provide more accurate and precise estimates of M_{BH} given a much larger sample of quasars at $3.20 \lesssim z \lesssim 3.50$, where both Mg II and H$\beta$ can be measured in the same near-infrared spectrum.

1. Introduction

A persisting point of interest in astrophysics today is understanding the coevolution of supermassive black holes (SMBHs) and their host galaxies through cosmic time (e.g., Hopkins et al. 2006; Di Matteo et al. 2008; Bromm & Yoshida 2011; Carniani et al. 2018; Chen et al. 2020; Suh et al. 2020). A fundamental ingredient in this research area is the SMBH mass (M_{BH}). Over the past four decades, several methods have been employed for obtaining M_{BH} values in galaxies (such as stellar kinematics, masers, interferometry, and spectrophotometric monitoring campaigns of active galaxies; e.g., Ferrarese & Merritt 2000; Gebhardt et al. 2000; Greene & Ho 2005; Gültekin et al. 2009; Greene et al. 2010; Shen et al. 2015; Grier et al. 2019; GRAVITY Collaboration et al. 2022). Overall, the masses obtained from these methods are consistent with each other, but deriving M_{BH} values in active galactic nuclei (AGNs) has the best prospects of obtaining the SMBH mass function through cosmic time given the large luminosities of such sources and their observable mass indicators at all accessible redshifts (e.g., Kelly et al. 2010; Kelly & Merloni 2012; Shen & Kelly 2012; Trakhtenbrot & Netzer 2012).

The M_{BH} values for AGNs, or quasars, are usually determined through measurements of broad emission lines in the optical band. Specifically, following the virial assumption (see Peterson & Wandel 1999), we use measurements of the size of the broad emission line region (BELR), R_{BELR}, and the velocity width of an emission line stemming from the BELR, ΔV, in order to estimate M_{BH} for AGNs. Of these terms, estimating the value of R_{BELR} becomes the most pertinent for reliable estimates of M_{BH}.

Ideally, measurements of R_{BELR} are derived from reverberation mapping (RM) of AGNs or quasars, which uses time lags between continuum fluctuations and photoionized BELR emission-line fluctuations to determine the size of the BELR

(e.g., Blandford & McKee 1982; Peterson 1993; Pancoast et al. 2014). To date, M_{BH} has been measured successfully using RM campaigns for ≈ 150 quasars primarily with the Hβ $\lambda 4861$ emission line (e.g., Barth et al. 2015; Bentz & Katz 2015; Grier et al. 2017; Du et al. 2018; Hu et al. 2021; Bao et al. 2022; U et al. 2022). One of the most important findings from these RM campaigns is the BELR size–luminosity (R–L) relation, where $R_{BELR} \propto L^{\alpha}$ with $\alpha \sim 0.5$, in agreement with expectations from photoionization theory (e.g., Laor 1998; Kaspi et al. 2000, 2005; Bentz et al. 2009, 2013).

Since RM campaigns are currently impractical for M_{BH} measurements in $\approx 10^6$ of known quasars (e.g., Shen et al. 2015), Vestergaard & Peterson (2006) have proposed that the R–L relation, in conjunction with the virial assumption, allows one to estimate single-epoch (SE) M_{BH} values by substituting the continuum luminosity for R_{BELR}. Estimates of M_{BH} values for $\approx 10^5$ quasars have been obtained in this fashion during the past two decades (e.g., Shen et al. 2011; Rakshit et al. 2020; Wu & Shen 2022).

Nevertheless, estimating M_{BH} values using the SE method faces additional challenges, particularly at high redshift. First, the most reliable SE indicator for M_{BH} is obtained from spectroscopic measurements of low-ionization emission lines such as the Hβ line, and at $z \gtrsim 1$, this line is shifted into the less accessible near-infrared (NIR) band. Second, recent super-Eddington accreting massive black hole (SEAMBH) and Sloan Digital Sky Survey-RM campaigns discovered many highly accreting objects that lie below the R–L relation (e.g., Du et al. 2018; Fonseca Alvarez et al. 2020), suggesting that an additional correction to account for accretion rate is warranted for SE M_{BH} estimates.

To overcome the first of these, SE M_{BH} estimates using other prominent emission lines have been calibrated against Hβ-based M_{BH} estimates in the nearby universe. The two most common emission lines that are used for such calibrations are Mg II $\lambda\lambda 2798$, 2803 (e.g., McLure & Dunlop 2004; Vestergaard & Osmer 2009; Zuo et al. 2015; Woo et al. 2018; Le et al. 2020) and C IV $\lambda 1549$ (e.g., Vestergaard & Peterson 2006; Assef et al. 2011; Runnoe et al. 2013; Brotherton et al. 2015; Coatman et al. 2017; Park et al. 2017; Sun et al. 2018; Dalla Bontà et al. 2020). However, these emission lines have yielded relatively fewer successful M_{BH} measurements through RM campaigns (e.g., Cackett et al. 2015; Shen et al. 2016; Lira et al. 2018; Grier et al. 2019; Hoormann et al. 2019; Homayouni et al. 2020; Kaspi et al. 2021), and each of these line profiles contains its own intrinsic measurement challenges (e.g., Vestergaard & Wilkes 2001; Baskin & Laor 2005). To address the second challenge, Du & Wang (2019) have proposed to include a correction to the R–L relationship based on the Fe II emission blend flanking the Hβ emission line, which is known to be an accretion-rate indicator. Recently, Maithil et al. (2022) implemented such a correction and found that M_{BH} estimates in highly accreting sources are overestimated.

In this work, we utilize a large spectroscopic inventory of high-redshift quasars that allows us to obtain the most reliable M_{BH} estimates using rest-frame ultraviolet (UV) emission lines. Our inventory includes high-quality measurements of the Hβ, Fe II, Mg II, and C IV emission lines, which allows us to implement two separate accretion-rate-based corrections to the estimated M_{BH} value while investigating the effects of using different BELR velocity width measurements.

This paper is organized as follows. In Section 2, we describe our sample and data analysis. In Section 3, we present the results of multiple regression analyses used for obtaining prescriptions for reliable M_{BH} estimates at high redshift. In Section 4 we discuss our results, and in Section 5 we present our conclusions. Throughout this paper, we compute luminosity distances using $H_0 = 70$ km s^{-1} Mpc^{-1}, $\Omega_M = 0.3$, and $\Omega_\Lambda = 0.7$ (e.g., Spergel et al. 2007).

2. Sample Selection and Measurements

Our sample is drawn from the Gemini Near Infrared Spectrograph–Distant Quasar Survey (GNIRS-DQS; Matthews et al. 2023, hereafter Paper I). Details of this survey, the data quality, and all spectral fits performed for each source are described in Matthews et al. 2021 (hereafter M21) and Paper I. Briefly, GNIRS-DQS utilizes spectroscopy from the GNIRS instrument (Elias et al. 2006) in the ~ 0.8–$2.5\mu m$ wavelength band at a spectral resolution of $R \sim 1100$ to construct the largest uniform rest-frame optical spectral inventory for high-redshift quasars (see M21). The GNIRS-DQS sources were selected from all the Sloan Digital Sky Survey (SDSS; York et al. 2000) quasars (Lyke et al. 2020) having m_i values up to ~ 19.0 that lie in the redshift intervals $1.55 \lesssim z \lesssim 1.65$, $2.10 \lesssim z \lesssim 2.40$, and $3.20 \lesssim z \lesssim 3.50$; these redshift intervals assure that the Hβ spectral region is covered in either the J, H, or K bands.

From all 260 GNIRS-DQS sources, we were able to practically measure C IV emission-line properties for 177 sources from their respective SDSS spectra. Typically, this emission line cannot be measured reliably in both broad absorption line (BAL) quasars and radio-loud (RL) quasars (RLQs).[15] Specifically, the C IV emission line is difficult to measure in BAL quasars due to BAL troughs often impacting the emission-line profile. Therefore, all 65 BAL quasars from the GNIRS-DQS sample were removed during our C IV-based M_{BH} estimate analysis. Additionally, since our analysis involves measurements of the rest-frame equivalent width (EW) of the C IV emission line, we further removed 16 RLQs from the sample. This was done in order to avoid potential dilution of the C IV emission line by continuum emission originating in the radio jets. We note that one of the BAL quasars we removed, SDSS J114705.24+083900.6, is also radio loud. Finally, we removed two sources, SDSS J073132.18+461347.0 and SDSS J141617.38+264906.1, for which we were unable to measure the C IV emission line reliably from their SDSS spectra. Specifically, the SDSS spectrum of J073132.18+461347.0 contains pixels with highly uncertain flux densities over a large portion of the C IV profile, while the spectrum of SDSS J141617.38+264906.1 suffers from significant narrow-line absorption, directly affecting the C IV profile, preventing us from obtaining a reliable line profile for both of these sources. The remaining sample of 177 non-BAL, non-RL sources with reliable C IV measurements was used in the C IV-based M_{BH} estimate analysis below.

The GNIRS spectra provide Mg II measurements for 99 of the GNIRS-DQS sources (see Paper I): only 70 of these sources also have corresponding C IV measurements following the removal of 22 BAL quasars and seven RLQs. From these 99

---

[15] We define RLQs as sources having radio-loudness values of $R > 100$ (where R is the ratio of the flux densities at 5 GHz and 4400 Å; Kellermann et al. 1989; Paper I).

quasars, 65 (47 with reliable C IV measurements) lie in the redshift range of $2.10 \lesssim z \lesssim 2.40$, and 34 (23 with reliable C IV measurements) lie at $3.20 \lesssim z \lesssim 3.50$. In both of these redshift ranges Mg II and Hβ are covered in the same spectrum; however, in the latter range, Mg II has the highest signal-to-noise (S/N) ratio (see Section 3.4 below, and see Zuo et al. 2015).

Furthermore, we were able to measure the Mg II profile in the SDSS spectra that adequately covered that emission line in 179 of the GNIRS-DQS sources: 34 and 13 of these sources do not have reliable C IV measurements given that these are BAL quasars and RLQs, respectively. From this sample of 179 quasars, 53 sources had a measurable Mg II profile in both the SDSS and the GNIRS-DQS spectra. When combining all available Mg II measurements, either from SDSS or GNIRS-DQS or both, we compiled a total sample of 225 sources: 47, 16, and 2 of these sources do not have reliable C IV measurements given that these are BAL quasars, RLQs, or sources without adequate C IV measurements, respectively.

2.1. Fitting the SDSS Spectra

The fitting procedure performed for the SDSS spectra in this work follows the methodology described in Dix et al. (2020). In short, this was done utilizing a local linear continuum and two Gaussians for each broad emission line. We find that fitting two Gaussians to the entire profile of the C IV and Mg II emission lines is sufficient given the S/N of ~40 per pixel across both the SDSS and GNIRS spectra. The Fe II and Fe III emission complex that blends with the Mg II emission line was modeled with the empirical template of Vestergaard & Wilkes (2001). This template was chosen for consistency between the Mg II fits presented in this work and those from Paper I. While this template does not account for Fe emission underlying the Mg II emission line, previous studies conclude this template over-estimates the Mg II FWHM intensity by up to ~20% (e.g., De Rosa et al. 2011; Onoue et al. 2020; Schindler et al. 2020; Yang et al. 2021). Overall, given the uncertainties of the Mg II emission-line measurements in the GNIRS spectra of our sources (see Paper I) and the intrinsic uncertainty of SE $M_{\rm BH}$ estimates (see Section 4), we expect any uncertainties associated with adopting this template to be modest for this analysis. This template was broadened with a Gaussian kernel having an FWHM intensity that was free to vary up to 10,000 km s^{-1} and was determined based on a least-squares analysis of each fitted region.

The Gaussians were constrained such that the flux density would lie between 0 and twice the value of the peak of the respective emission line, and the FWHM was restricted to lie within 0 and 15000 km s^{-1}. The peaks of these Gaussians were also constrained to lie within ± 1500 km s^{-1} of the rest-frame wavelength of the peak of the emission line based on the systemic redshift from Paper I. After the initial fitting was performed for each region, we visually inspected the fit to see if more lenient constraints with interactive fitting were warranted.

We excluded BAL quasars and RLQs throughout this work in order to avoid potentially large uncertainties in the properties of the C IV emission line, as described above. However, our derived prescriptions should be applicable to any quasar, given that a C IV emission line can be measured reliably in its spectrum.

Spectral properties stemming from these fits are reported in Table 1 for C IV and Mg II. In this table, Column (1) reports the

source's SDSS designation. Columns (2), (3), (4), (5), and (6) list the FWHM; mean absolute deviation (MAD; described below in Section 2.2); line dispersion ($\sigma_{\rm line}$); rest-frame EW; and the observed-frame wavelength of the emission-line peak, $\lambda_{\rm peak}$, respectively, for C IV. Columns (7), (8), (9), (10), and (11) list the same spectral properties for the Mg II emission line.

2.2. Measurements and Error

For each emission-line profile in either the GNIRS or SDSS spectra, we measured the values of the $\sigma_{\rm line}$ and MAD. The line dispersion is defined by

$$\sigma_{\rm line} = \left[\frac{\int (\lambda - \lambda_0)^2 P(\lambda) d\lambda}{\int P(\lambda) d\lambda} \right]^{1/2}, \qquad (1)$$

where λ_0 is the line centroid and $P(\lambda)$ is the emission-line profile. The MAD is defined as

$$\mathrm{MAD} = \int |\lambda - \lambda_{\rm med}| P(\lambda) d\lambda \Big/ \int P(\lambda) d\lambda, \qquad (2)$$

where $\lambda_{\rm med}$ is the median wavelength of the emission-line profile, first suggested in Denney et al. (2016) as an appropriate representation for the emission-line width. For each emission-line profile in the GNIRS spectra, we obtained the FWHM, EW, and observed-frame wavelength of the peak emission from Paper I.

We present three different values for the velocity widths (FWHM, MAD, and $\sigma_{\rm line}$) due to the uncertainties inherent in using FWHM, the most popular of these parameters (see Park et al. 2017; Dalla Bontà et al. 2020; Le et al. 2020). While $\sigma_{\rm line}$ is a dependable measurement to describe the emission-line velocity width, Denney et al. (2016) suggest that MAD provides a more accurate estimate of this quantity for low-quality data. Overall, we recognize that the best virial velocity width indicator is debatable; therefore, we provide calibrations for the $M_{\rm BH}$ estimates utilizing all of these parameters.

We have also derived the monochromatic luminosities, L_{1350} and L_{3000}, by measuring the continuum flux densities at rest-frame $\lambda 1350$ Å and $\lambda 3000$ Å, respectively, and employing our chosen cosmology. All the flux densities and monochromatic luminosities at rest-frame $\lambda 5100$ Å (L_{5100}) used in this work were obtained from Paper I. The flux calibration for the GNIRS-DQS spectra is extensively discussed in M21. In our $z < 1.65$ sources, the flux density at rest-frame wavelength 3000 Å was not measurable in the GNIRS-DQS spectrum due to this wavelength range falling blueward of the J band. In these cases, the flux density was determined by extrapolating from the flux density at rest-frame wavelength 5100 Å using the canonical quasar optical-UV continuum of the form $f_\nu \propto \nu^{-0.5}$ (e.g., Richstone & Schmidt 1980; Vanden Berk et al. 2001). Similarly, there are SDSS spectra that do not have a reliable flux density value for the rest-frame wavelength 1350 Å due to low S/N at the blue end of the SDSS spectrum. In these cases, we employed the same model as described above extrapolating from the flux density at rest-frame 1450 Å.

The uncertainties for all emission-line measurements reported in Table 1 were determined by following the methods described in M21 and Paper I. Briefly, we created mock spectra that introduced random Gaussian noise to the original spectra. We then fit these spectra as described above and measured the newly fit profiles. This process was repeated 1000 times in

Table 1
C IV and Mg II Spectroscopic Measurements

	C IV					Mg II						
Quasar	FWHM (km s^{-1})	MAD (km s^{-1})	σ_{line} (km s^{-1})	EW (Å)	λ_{peak} (Å)	FWHM (km s^{-1})	MAD (km s^{-1})	σ_{line} (km s^{-1})	EW (Å)	λ_{peak} (Å)	log($\lambda L_{1350\text{Å}}$) (erg s^{-1})	log($\lambda L_{3000\text{Å}}$) (erg s^{-1})
(1)	(2)	(3)	(4)	(5)	(6)	(7)	(8)	(9)	(10)	(11)	(12)	(13)
SDSS J001018.88+280932.5	2517^{+53}_{-78}	2274^{+37}_{-54}	3158^{+55}_{-82}	61^{+1}_{-1}	4045^{+0}_{-0}	⋯	⋯	⋯	⋯	⋯	46.4	⋯
SDSS J001249.89+285552.6	⋯	⋯	⋯	⋯	⋯	4195^{+188}_{-249}	2183^{+480}_{-757}	2956^{+637}_{-1017}	21^{+7}_{-9}	11874^{+3}_{-5}	⋯	46.9
SDSS J001355.10-012304.0	⋯	⋯	⋯	⋯	⋯	2815^{+344}_{-455}	1249^{+260}_{-401}	1595^{+332}_{-515}	17^{+1}_{-2}	12274^{+4}_{-5}	⋯	46.7
SDSS J001453.20+091217.6	6487^{+822}_{-1227}	3798^{+910}_{-1358}	5788^{+1383}_{-2064}	39^{+3}_{-5}	5152^{+5}_{-7}	2999^{+943}_{-1248}	1833^{+1906}_{-1833}	2375^{+2580}_{-2375}	25^{+8}_{-11}	9374^{+8}_{-10}	46.4	46.5
SDSS J001813.30+361058.6	6079^{+197}_{-294}	3247^{+238}_{-356}	3861^{+369}_{-550}	26^{+1}_{-2}	5116^{+2}_{-3}	5129^{+983}_{-1301}	3354^{+1648}_{-2632}	4543^{+2198}_{-3511}	25^{+8}_{-11}	9303^{+13}_{-17}	46.8	46.6
SDSS J001914.46+155555.9	4162^{+215}_{-320}	2329^{+81}_{-120}	3038^{+121}_{-180}	45^{+1}_{-1}	5054^{+1}_{-2}	4380^{+327}_{-433}	1628^{+821}_{-1235}	2061^{+1092}_{-1643}	23^{+1}_{-1}	9141^{+5}_{-6}	46.7	46.5
SDSS J002634.46+274015.5	5196^{+739}_{-1103}	6331^{+868}_{-1295}	6701^{+1462}_{-2181}	135^{+10}_{-15}	5023^{+5}_{-7}	3158^{+150}_{-198}	1747^{+645}_{-979}	2373^{+934}_{-1418}	36^{+1}_{-1}	9097^{+2}_{-2}	46.2	46.5
SDSS J003001.11-015743.5	6077^{+265}_{-396}	3339^{+251}_{-374}	3719^{+449}_{-669}	53^{+2}_{-3}	3995^{+1}_{-2}	⋯	⋯	⋯	⋯	⋯	45.9	⋯
SDSS J003416.61+002241.1	4213^{+107}_{-160}	2092^{+43}_{-65}	2710^{+66}_{-98}	29^{+0}_{-0}	4067^{+1}_{-1}	4141^{+203}_{-269}	1767^{+233}_{-308}	2278^{+414}_{-548}	39^{+2}_{-2}	7366^{+2}_{-2}	46.4	46.4
SDSS J003853.15+333044.3	8273^{+564}_{-841}	2485^{+403}_{-602}	3817^{+593}_{-884}	14^{+1}_{-1}	5213^{+11}_{-17}	⋯	⋯	⋯	⋯	⋯	46.3	⋯

Note. C IV and Mg II emission-line measurements for the first ten quasars in our sample.

(This table is available in its entirety in machine-readable form.)

order to obtain a distribution for each of our parameters, and the 68% range is reported as our measurement uncertainty.

3. UV-based Black Hole Mass Calibration

3.1. Estimating Black Hole Masses

In order to perform the analysis discussed in this work, we must first establish Hβ-based $M_{\rm BH}$ estimates (obtained from Paper I), followed by an outline for developing prescriptions for the C IV- and Mg II-based $M_{\rm BH}$ estimates. The initial step is to obtain SE $M_{\rm BH}$ estimates for each emission line following the virial assumption,

$$M_{\rm BH} = \frac{f R_{\rm BELR} \Delta V^2}{G}, \qquad (3)$$

where G is the gravitational constant and f is the virial factor, which depends on the geometry and orientation of the system and is assumed to be on the order of ≈ 1 (e.g., Ho & Kim 2014; Yu et al. 2019). The next step is to substitute the continuum luminosity for $R_{\rm BELR}$ according to the R–L relation (see Section 1) as $R_{\rm BELR} \propto L^{0.5}$.

We estimate Hβ-based $M_{\rm BH}$ values by further correcting the $R_{\rm BELR}$ parameter in Equation (3) (hereafter $R_{\rm H\beta}$) for the source accretion rate, based on the scaling relation presented in Du & Wang (2019) in the following way

$$\log(R_{\rm H\beta}/{\rm lt - days}) = \alpha + \beta \log \ell_{44} + \gamma \mathcal{R}_{\rm Fe}, \qquad (4)$$

where $\ell_{44} = L_{5100}/10^{44}$ erg s^{-1}, $\alpha = 1.65 \pm 0.06$, $\beta = 0.45 \pm 0.03$, $\gamma = -0.35 \pm 0.08$, and $\mathcal{R}_{\rm Fe}$ is an indicator of the strength of the Fe II emission defined as the ratio of the flux (F) or EW between Fe II (in the 4434-4684 Å rest-frame band; Boroson & Green 1992) and Hβ: $\mathcal{R}_{\rm Fe} = F_{\rm Fe\,II}/F_{\rm H\beta} \approx {\rm EW}_{\rm Fe\,II}/{\rm EW}_{\rm H\beta}$. In this work we employ the ratio of EWs to determine $\mathcal{R}_{\rm Fe}$. For the virial factor in Equation (3), we adopt $f = 1.5$ and the FWHM as ΔV for Hβ-based $M_{\rm BH}$ values (Maithil et al. 2022). The value of the f factor introduces additional uncertainty, on the order of ~ 2–3 (e.g., Mejía-Restrepo et al. 2018), in our estimation of $M_{\rm BH}$. Our adopted value is consistent with Yu et al. (2020) and the emipirical best-fit value obtained from the M–$\sigma_\star$ correlation (e.g., Onken et al. 2004; Ho & Kim 2014; Woo et al. 2015).

Maithil et al. (2022) have shown that this accretion-rate correction is necessary for adjusting $M_{\rm BH}$ values that are overestimated by a factor of ~ 2 for typical luminous high-redshift quasars. We compare the accretion-rate-corrected Hβ-based $M_{\rm BH}$ estimates for our sample to the traditional approach of Vestergaard & Peterson (2006, hereafter VP06), which uses the following equation to obtain Hβ-based $M_{\rm BH}$ values:

$$\log\left(\frac{M_{\rm BH}}{M_\odot}\right) = 0.91 + 2\log\left(\frac{{\rm FWHM}_{\rm H\beta}}{{\rm km\ s}^{-1}}\right)$$
$$+ 0.5\log\left(\frac{\lambda L_\lambda(5100\ {\rm Å})}{10^{44}{\rm erg\ s}^{-1}}\right), \qquad (5)$$

utilizing a virial factor on the order of unity. Figure 1 presents the Hβ-based $M_{\rm BH}$ masses for our sample, based on the relation of VP06 against our accretion-rate-corrected values. We find that the masses, computed according to the VP06 approach, are systematically overestimated by 0.26 dex. This result is consistent with the findings in Maithil et al. (2022).
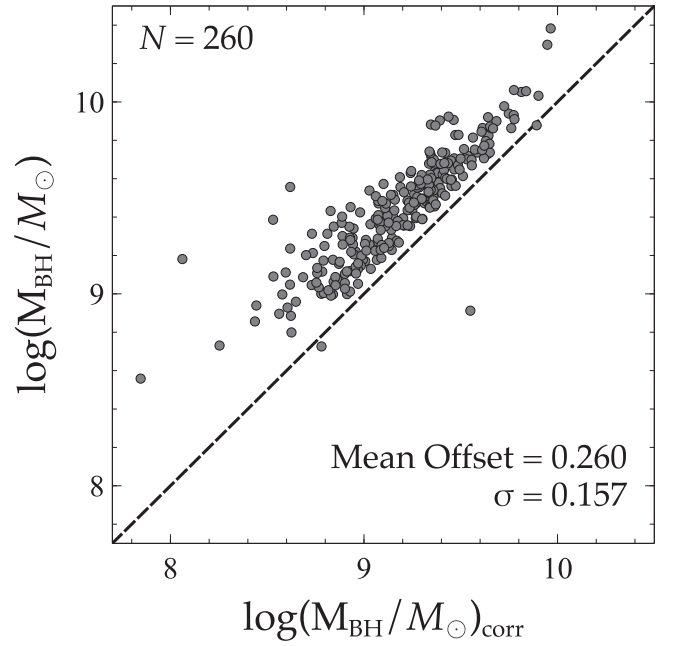

Figure 1. The Hβ-based $M_{\rm BH}$ estimates of all 260 quasars from the GNIRS-DQS sample calculated using the VP06 approach (y-axis) and correcting for accretion rate (x-axis). The dashed line represents a one-to-one relationship. This figure shows that Hβ-based $M_{\rm BH}$ estimates that were not corrected for accretion rate are systematically overestimated.

Given that correcting for accretion rate is necessary for accurate $M_{\rm BH}$ estimates, we explore whether additional accretion-rate-based corrections would further improve $M_{\rm BH}$ estimates for rest-frame UV emission lines. To accomplish this, we introduce a term into our UV-based $M_{\rm BH}$ estimates that includes the C IV EW as this parameter has been shown to be generally anticorrelated with the quasar's accretion rate (e.g., Baskin & Laor 2004; Shemmer & Lieber 2015). Another C IV observable property that is known to be related to the accretion rate is the emission-line blueshift with respect to a source-systemic redshift (e.g., Baskin & Laor 2005; Ha et al. 2023, hereafter Paper III). However, this property cannot be measured reliably when a corresponding indicator of $z_{\rm sys}$ (e.g., the [O III] λ 5007 emission line) is unavailable. Since our prescriptions for obtaining UV-based $M_{\rm BH}$ estimates are not restricted to the availability of such indicators, we do not introduce an additional accretion-rate correction term based on C IV blueshift.

Following Equation (3), assuming $R_{\rm BELR} \propto L^{0.5}$, with the addition of a C IV EW term, we derive our C IV-based $M_{\rm BH}$ estimates as

$$\log\left(\frac{M_{\rm BH}}{M_\odot}\right) = 2\log\left(\frac{\Delta V}{10^3\ {\rm km\ s}^{-1}}\right) + 0.5\log\left(\frac{\lambda L_\lambda(1350\ {\rm Å})}{10^{44}{\rm erg\ s}^{-1}}\right)$$
$$+ a + b\log\left(\frac{{\rm EW}_{\rm C\,IV}}{{\rm Å}}\right). \qquad (6)$$

The coefficients a and b were determined from a linear-regression analysis to the calibration set of ($R_{\rm Fe\,II}$ corrected) Hβ-based $M_{\rm BH}$ estimates. By design, we allow a and b to freely vary during the regression analysis, resulting in a zero mean offset between the C IV-based and Hβ-based $M_{\rm BH}$ estimates.
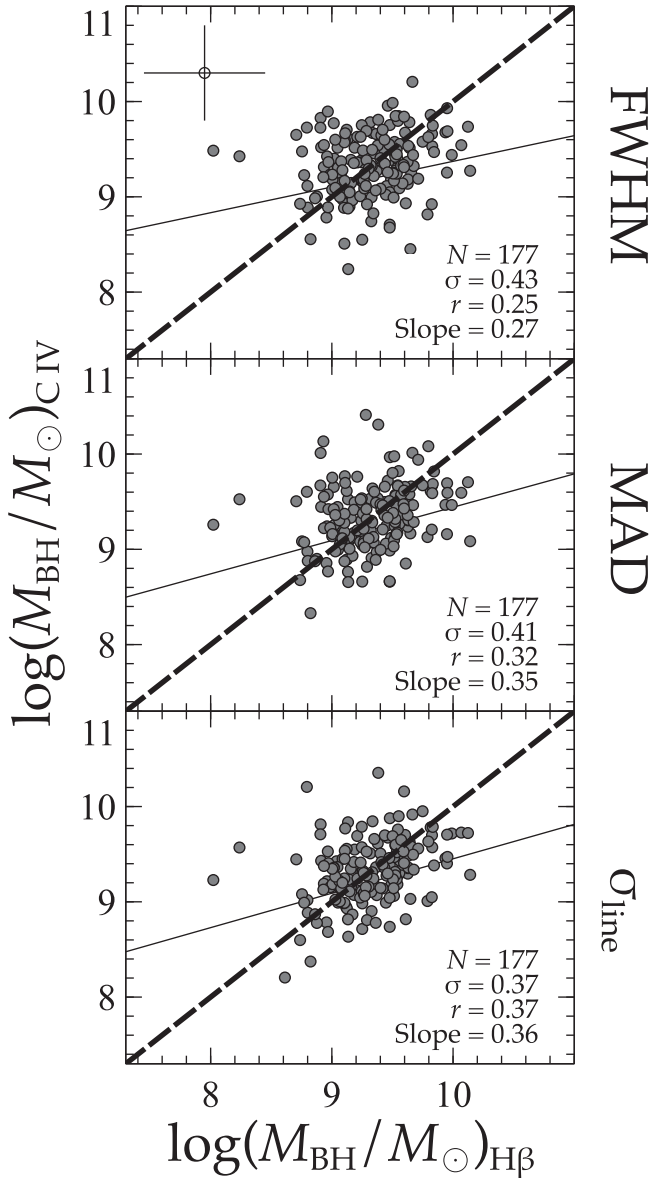
Figure 2. The calibrated C IV-based $M_{\rm BH}$ estimates using the three velocity width parameters, discussed in Section 3.1, against the calibration set of Hβ-based $M_{\rm BH}$ estimates. The dashed line in each panel represents a one-to-one relationship, and the thin solid line in each panel represents the best linear fit to the data. The Pearson correlation coefficient (r) and the slope of the best-fit line are provided in each panel. Notably, using $\sigma_{\rm line}$ as the velocity width parameter provides the most precise C IV-based $M_{\rm BH}$ estimates with respect to the Hβ-based $M_{\rm BH}$ estimates. Additionally, using $\sigma_{\rm line}$ as the velocity width parameter leads to the largest Pearson correlation coefficient and steepest slope of the best-fit relation. Typical uncertainty of 0.5 dex on the $M_{\rm BH}$ values is displayed in the top panel for reference.

The linear regression was performed such that the difference between our C IV-based $M_{\rm BH}$ values and the Hβ-based $M_{\rm BH}$ values was minimized. Specifically, we subtracted the first two terms in Equation (6) from the derived Hβ-based $M_{\rm BH}$ estimates and fit the remaining coefficients, a and b, to this difference. This was accomplished utilizing the REGSTATS function in the Statistics Toolbox 11.4 of MATLAB 9.5. As the errors associated with SE $M_{\rm BH}$ values are large (on the order of 0.5–0.6 dex and 0.7 dex for relative and absolute uncertainty, respectively; see Section 4), we did not include the errors as part of the linear regression. Despite this, we also employed the

LINMIX_ERR algorithm (Kelly 2007) where we adopted a 0.5 dex uncertainty to have a basis of comparison for our regression and found the results were generally consistent. The uncertainty of the coefficients, presented in our equations below, stems directly from the linear fit.

Our next step is to focus on $M_{\rm BH}$ estimates that utilize the Mg II emission line. Unlike the case for C IV above, we calibrate our Mg II-based $M_{\rm BH}$ estimates in two separate runs using the following equation,

$$\log\left(\frac{M_{\rm BH}}{M_\odot}\right) = 2\log\left(\frac{\Delta V}{10^3\,{\rm km\,s^{-1}}}\right) + 0.5\log\left(\frac{\lambda L_\lambda(3000\,{\rm \AA})}{10^{44}{\rm erg\,s^{-1}}}\right)$$
$$+ c + d\log\left(\frac{{\rm EW}_{\rm C\,IV}}{\rm \AA}\right),$$

(7)

where ΔV is the velocity width of Mg II; the Mg II lines were measured from a combination of the SDSS and GNIRS spectra of the sources as described below in Section 3.4. The coefficients c and d were determined differently in each run through a linear-regression analysis to the calibration set of Hβ-based $M_{\rm BH}$ estimates. The first run set the coefficient d to 0 in order to provide a prescription that only used the Mg II emission line while allowing c to be a free parameter. For this run we did not need any C IV measurements, allowing us to use all of the Mg II measurements in each subsample (see Section 2). The second run allowed both c and d to vary freely during the regression. This run required C IV measurements, reducing our Mg II sample as described in Section 2. In both runs, we used the same type of linear regression as discussed for the C IV analysis.

Given the considerably lower S/N ratio of the GNIRS spectra at $\lambda \lesssim 1.2\,\mu{\rm m}$ (M21), we split the analysis utilizing the Mg II line measured from the GNIRS spectra into three different parts based on source redshift (see Section 2). In addition to these subsamples, we analyzed the total of 160 and 225 sources for the subsample including all Mg II measurements (whether from SDSS or GNIRS) with and without C IV, respectively. For the subsample of 53 sources that have Mg II measurements available in both the GNIRS and SDSS spectra, the average of these measurements was used in the regression analyses (see Section 3.4).

3.2. Testing Different Velocity Width Parameters

We substitute the FWHM, MAD, and $\sigma_{\rm line}$ as the velocity width parameter in each of our $M_{\rm BH}$ estimates in Equations (6) and (7) to further investigate which of these parameters provides $M_{\rm BH}$ values closest to those obtained from Hβ. In each analysis described above, we calibrate the C IV- and Mg II-based $M_{\rm BH}$ estimates to the Hβ-based values that use the FWHM for the velocity width of Hβ (Maithil et al. 2022). We determined which velocity width parameter was preferred based on the lowest standard deviation, steepest slope of the best-fit relation, and largest Pearson correlation coefficient when comparing the resulting UV- and Hβ-based $M_{\rm BH}$ values. For the C IV-based $M_{\rm BH}$ estimates, presented in Figure 2, the $\sigma_{\rm line}$ produced the most precise results when compared to the Hβ-based $M_{\rm BH}$ values.

For each of the Mg II subsamples described above, we present the calibrated Mg II-based $M_{\rm BH}$ estimates in Figures 3,
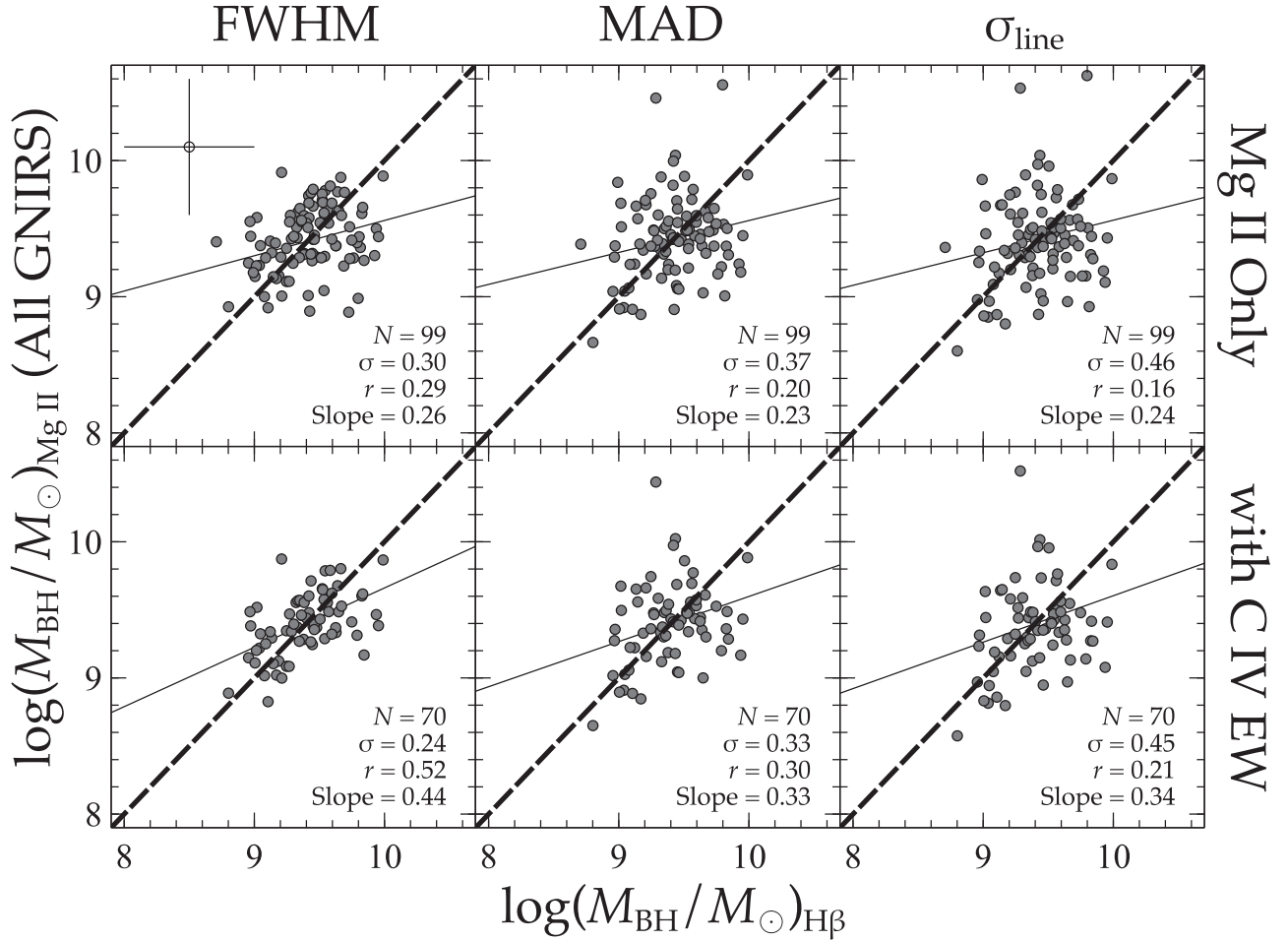
Figure 3. Calibrated Mg II-based M_{BH} estimates using the three velocity width parameters against the Hβ-based M_{BH} estimates; the bottom panels present the results when adding EW(C IV) to the analysis as discussed in Section 3.1. The symbols are the same as in Figure 2. For all the Mg II-based M_{BH} estimates, using the FWHM as the velocity width parameter provided the most precise results when compared to the Hβ-based M_{BH} estimates. For all velocity width parameters, the inclusion of the EW(C IV) parameter improves the precision of the relation, demonstrated by a reduction in the scatter and an increase in the correlation coefficient in each case. Typical uncertainty of 0.5 dex on the M_{BH} values is displayed in the top left panel for reference.

4, 5, and 6 both with (bottom panels) and without (top panels) the inclusion of the C IV EW. Except for the subsample of sources at $3.20 \lesssim z \lesssim 3.50$, all the other Mg II-based subsamples showed the strongest correlation with the Hβ-based M_{BH} estimates when using the FWHM as the velocity width parameter for the Mg II line. For the subsample at $3.20 \lesssim z \lesssim 3.50$, we find that using the MAD for the velocity width parameter in M_{BH} estimates provides the best results when using only the Mg II emission line (see Figure 5). We recognize that this discrepancy may be a result of the limited sample size, which may not provide meaningful statistics. In spite of this, the results from this subsample are considered to be the least uncertain given that Mg II and Hβ are measured in the same spectrum with the highest S/N ratio possible. The best-fit coefficients stemming from our linear-regression analyses appear in Table 2.

3.3. Comparison with Previous Studies

In order to have a basis of comparison for this work, we provide estimates for the C IV-based M_{BH} values for our sample using the prescriptions provided in VP06 (Park et al. 2017, hereafter P17) and (Coatman et al. 2017, hereafter C17). VP06, P17, and C17, use the following equations to determine

C IV-based M_{BH} estimates, respectively,

$$\log\left(\frac{M_{BH}}{M_\odot}\right) = 6.66 + 2.0\log\left(\frac{FWHM_{CIV}}{10^3\ km\ s^{-1}}\right)$$
$$+ 0.53\log\left(\frac{\lambda L_\lambda(1350\ Å)}{10^{44} erg\ s^{-1}}\right), \quad (8)$$

$$\log\left(\frac{M_{BH}}{M_\odot}\right) = 6.73 + 2.0\log\left(\frac{\sigma_{line,CIV}}{10^3\ km\ s^{-1}}\right)$$
$$+ 0.43\log\left(\frac{\lambda L_\lambda(1350\ Å)}{10^{44} erg\ s^{-1}}\right), \quad (9)$$

$$\log\left(\frac{M_{BH}}{M_\odot}\right) = 6.71 + 2.0\log\left(\frac{FWHM_{C\,IV,Corr.}}{10^3\ km\ s^{-1}}\right)$$
$$+ 0.53\log\left(\frac{\lambda L_\lambda(1350\ Å)}{10^{44} erg\ s^{-1}}\right). \quad (10)$$

VP06 uses the FWHM as the velocity width, while P17 uses σ_{line}. C17 uses a velocity width ($FWHM_{C\,IV,Corr.}$) that has been adjusted by the blueshift of the C IV emission-line peak with respect to the line peak of Hβ (see Coatman et al. 2017). When
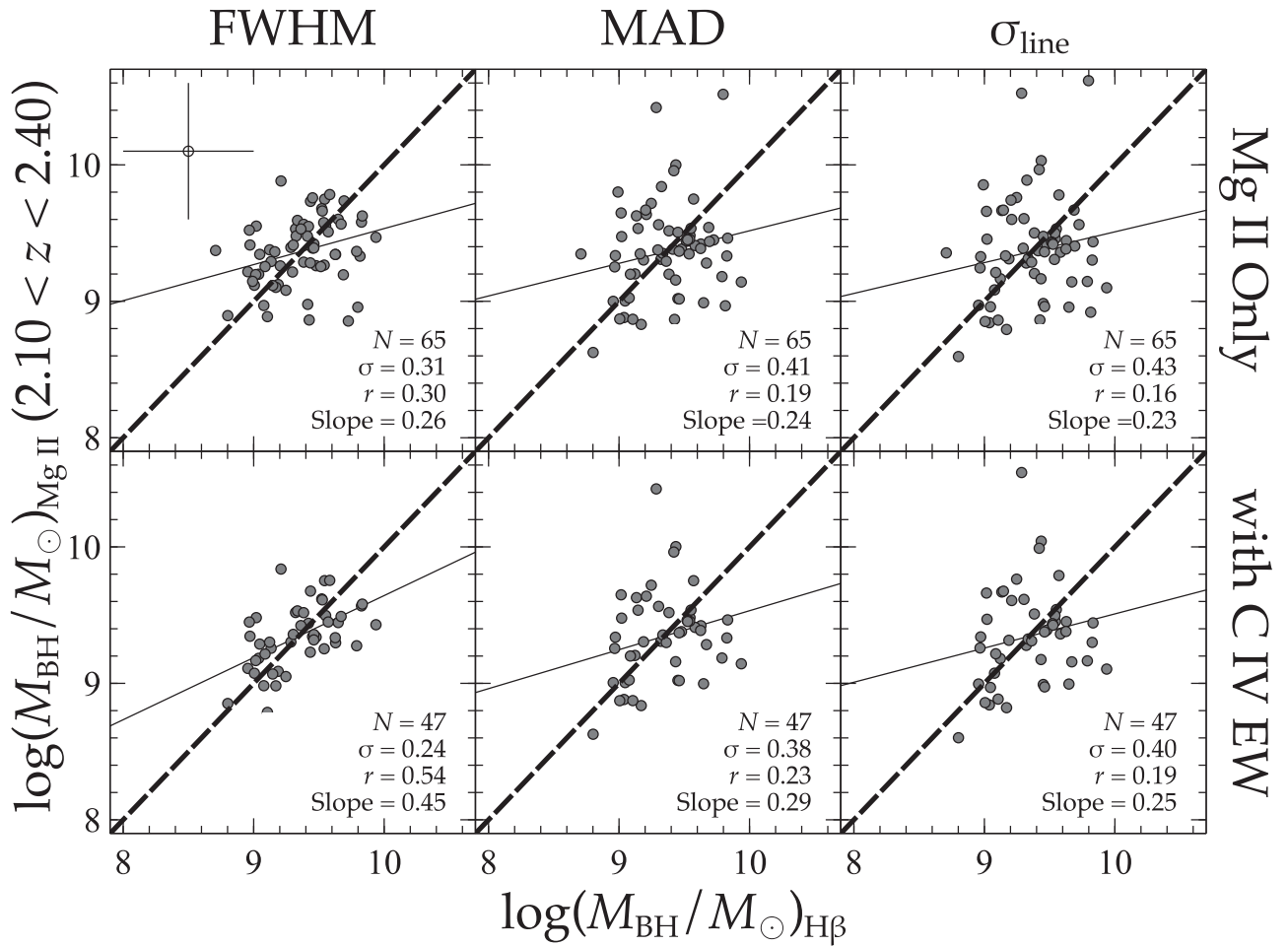
Figure 4. Same as Figure 3 but for the subset of sources in the range $2.10 \lesssim z \lesssim 2.40$. As observed for the entire redshift range (Figure 3), the FWHM of Mg II is the most reliable velocity width parameter, and the inclusion of the C IV EW helped improve the precision of the Mg II-based M_{BH} estimates with respect to those obtained from Hβ.

evaluating these relations alongside the C IV-based prescription derived in this work, we compare them to the Hβ-based M_{BH} estimates using the FWHM as the velocity width parameter; see Section 3.1.

In Figure 7 we present the C IV-based M_{BH} estimates for our sample based on the prescriptions from the literature. In comparison, our prescription,

$$\log\left(\frac{M_{BH}}{M_\odot}\right) = (6.299 \pm 0.169) + 2\log\left(\frac{\sigma_{line}}{10^3 \text{ km s}^{-1}}\right)$$
$$+ 0.5\log\left(\frac{\lambda L_\lambda(1350\text{ Å})}{10^{44}\text{erg s}^{-1}}\right) + (0.385 \pm 0.119)\log\left(\frac{\text{EW}_{CIV}}{\text{Å}}\right),$$
$$(11)$$

which is plotted at the bottom panel of Figure 2, provides the smallest scatter, steepest slope of the best-fit relation, largest Pearson correlation coefficient, and, by design, corrects the mean offset[16] between previous C IV-based M_{BH} estimates and the Hβ-based M_{BH} value.

To form a basis of comparison for our Mg II-based M_{BH} estimates, we followed the prescriptions provided in

Vestergaard & Osmer (2009, hereafter VO09), Zuo et al. (2015, hereafter Z15), and Le et al. (2020, hereafter L20). VO09, Z15, and L20 use the following equations to determine Mg II-based M_{BH} estimates, respectively,

$$\log\left(\frac{M_{BH}}{M_\odot}\right) = 0.86 + 2.0\log\left(\frac{\text{FWHM}_{MgII}}{\text{km s}^{-1}}\right)$$
$$+ 0.5\log\left(\frac{\lambda L_\lambda(3000\text{ Å})}{10^{44}\text{erg s}^{-1}}\right),$$
$$(12)$$

$$\log\left(\frac{M_{BH}}{M_\odot}\right) = 1.07 + 2.0\log\left(\frac{\text{FWHM}_{MgII}}{\text{km s}^{-1}}\right)$$
$$+ 0.48\log\left(\frac{\lambda L_\lambda(3000\text{ Å})}{10^{44}\text{erg s}^{-1}}\right),$$
$$(13)$$

$$\log\left(\frac{M_{BH}}{M_\odot}\right) = 7.00 + 2.0\log\left(\frac{\text{FWHM}_{MgII}}{10^3 \text{ km s}^{-1}}\right)$$
$$+ 0.5\log\left(\frac{\lambda L_\lambda(3000\text{ Å})}{10^{44}\text{erg s}^{-1}}\right).$$
$$(14)$$

In Figure 8, we present the Mg II-based M_{BH} estimates from Equations (12), (13), and (14). The three panels of Figure 8 that correspond to these three equations are almost identical to each

────────────

[16] The mean-offset correction accounts for the bias introduced when not considering a source's accretion rate in its Hβ-based M_{BH} value (see Maithil et al. 2022).
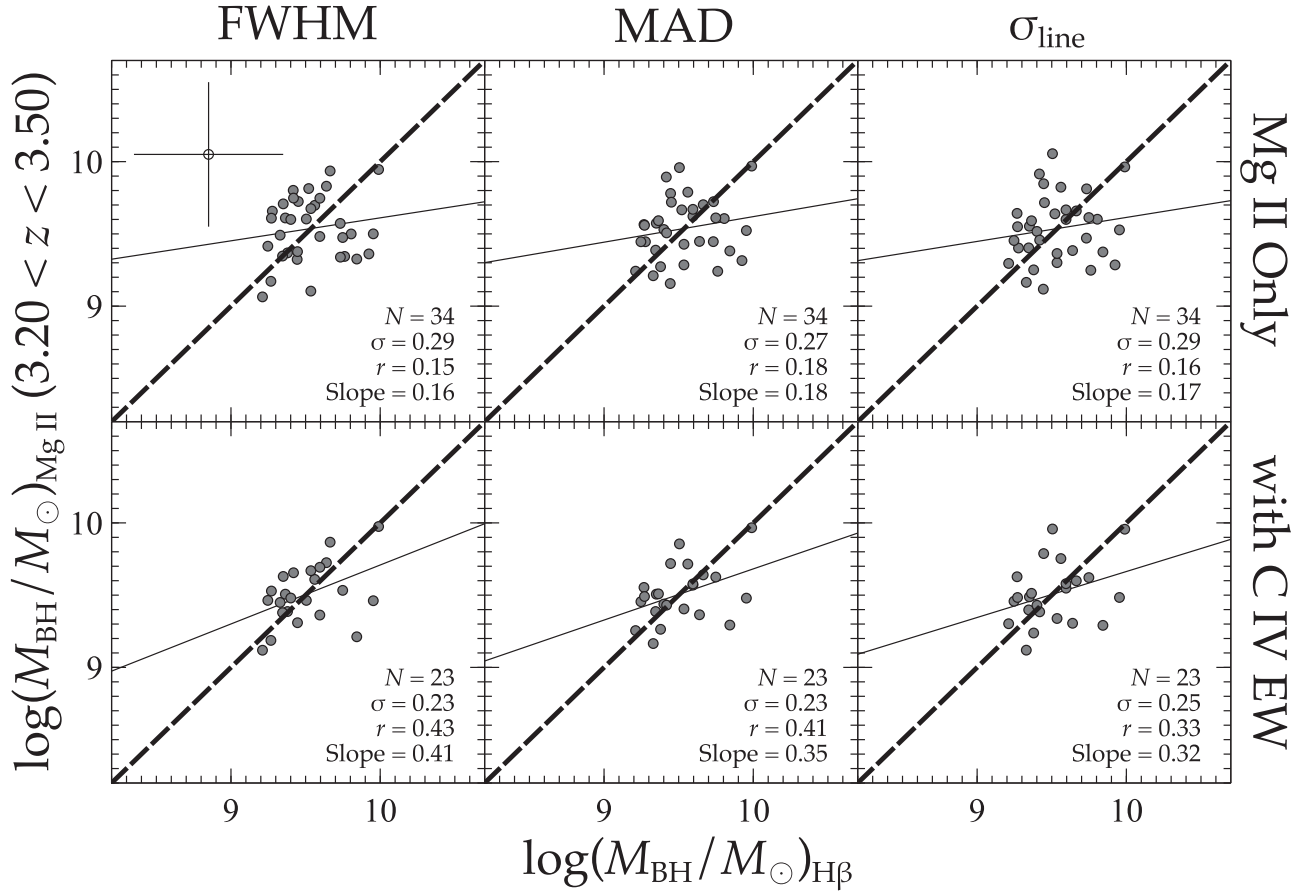
Figure 5. Same as Figure 3 but for the subset of sources in the range $3.20 \lesssim z \lesssim 3.50$. In this subset of sources the most reliable velocity width parameter for deriving Mg II only based M_{BH} estimates is the MAD instead of the FWHM. This is determined from evaluating the standard deviations and r in each panel. This disparity suggests the importance of expanding the sample of quasars that lie in this redshift range. As we find for the entire redshift range, the inclusion of the EW of C IV (bottom panels) improves the precision of these Mg II-based M_{BH} estimates.

other given the similarities between these equations. For comparison, we elect to use the Mg II subsample that contains SDSS and/or GNIRS measurements as it is the largest and therefore provides the most meaningful statistics. From our comparison, we find that our Mg II-based M_{BH} estimates given by

$$\log\left(\frac{M_{BH}}{M_\odot}\right) = (7.000 \pm 0.022) + 2\log\left(\frac{\mathrm{FWHM_{Mg\,II}}}{10^3\,\mathrm{km\,s^{-1}}}\right)$$
$$+ 0.5\log\left(\frac{\lambda L_\lambda(3000\,\text{Å})}{10^{44}\mathrm{erg\,s^{-1}}}\right), \qquad (15)$$

which are plotted at the top left panel of Figure 6, provide results that are consistent with those from the prescriptions of the previous studies except for the mean-offset correction stemming from consideration of the accretion rate. The consistency between Equations (14) and (15) confirms the results derived in L20.

When the C IV EW is included in the regression analysis for the Mg II-based M_{BH} values, we obtain the following

prescription (for 160 sources; see Section 2),

$$\log\left(\frac{M_{BH}}{M_\odot}\right) = (6.793 \pm 0.047) + 2\log\left(\frac{\mathrm{FWHM_{MgII}}}{10^3\,\mathrm{km\,s^{-1}}}\right)$$
$$+ 0.5\log\left(\frac{\lambda L_\lambda(3000\,\text{Å})}{10^{44}\mathrm{erg\,s^{-1}}}\right)$$
$$+ (0.005 \pm 0.001)\log\left(\frac{\mathrm{EW_{CIV}}}{\text{Å}}\right), \qquad (16)$$

which is plotted in the bottom left panel of Figure 6. In this case, we see a clear improvement in the scatter, the Pearson correlation coefficient, and slope of the best-fit relation.

We report all the M_{BH} estimates for the Hβ, C IV, and Mg II lines in Table 3 where Column (1) provides the SDSS designation of the object and Columns (2), (3), and (4) provide the Hβ-based M_{BH} estimates derived using the FWHM, MAD, and σ_{line} as the velocity width, respectively. Columns (5), (6), and (7) provide C IV-based M_{BH} estimates derived from VP06, P17, and C17, respectively. Columns (8), (9), and (10) are the C IV-based estimates derived using the regression analysis for each C IV velocity width parameter, FWHM,
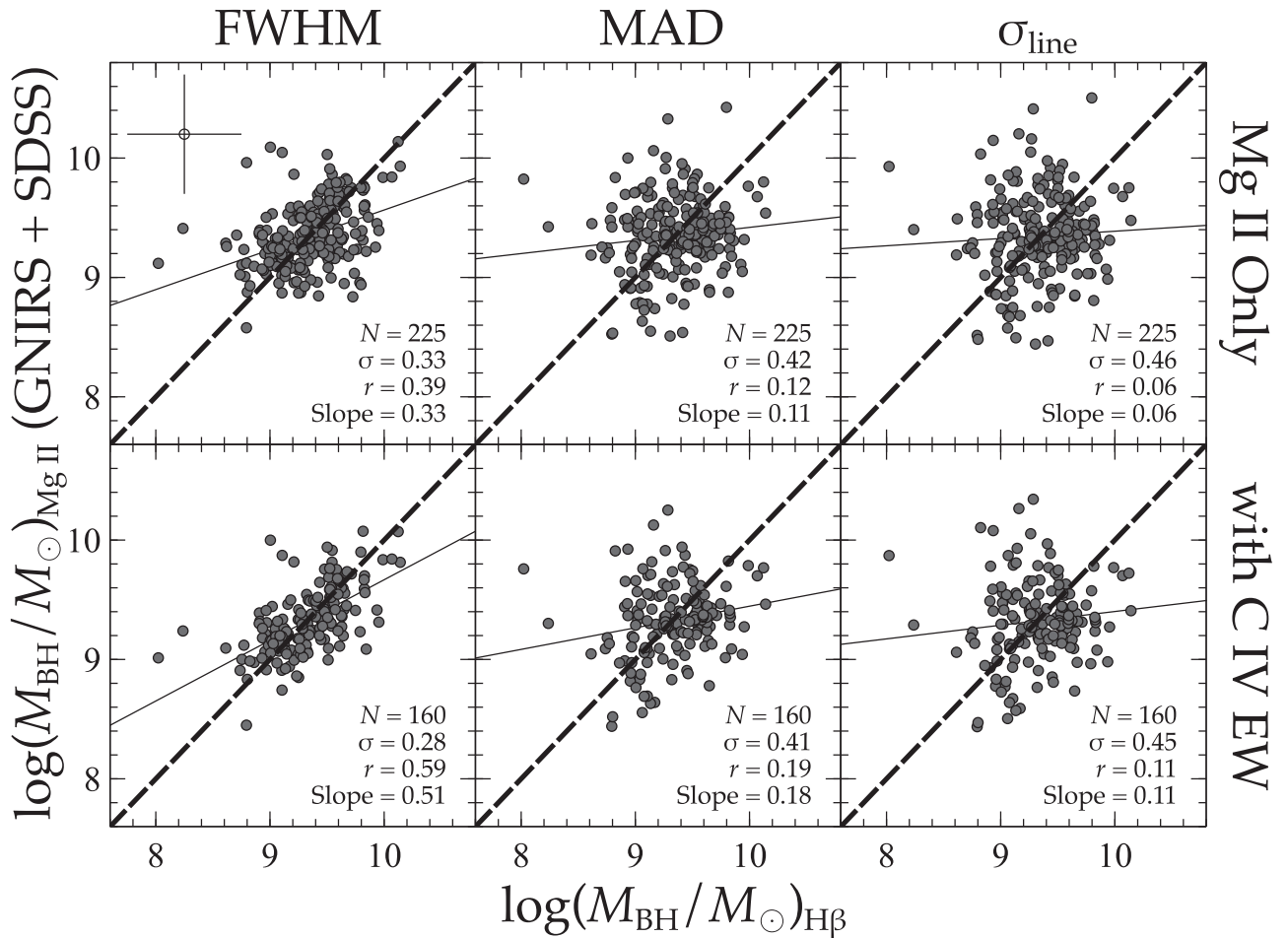
Figure 6. Same as Figure 3 but for the source sample having Mg II measurements taken from GNIRS-DQS and/or SDSS. From evaluating the standard deviations and Pearson correlation coefficients in each panel, we find that using the FWHM as the velocity width parameter in the calculation for Mg II-based M_{BH} estimates provides the most precise M_{BH} estimates with respect to the Hβ-based M_{BH} values. As we find for each Mg II subsample, the inclusion of the EW of C IV (bottom panels) improves the precision of our Mg II-based M_{BH} estimates even more.

MAD, and σ_{line}, respectively. We report in columns (11), (12), and (13) the Mg II-based M_{BH} estimates derived using the prescriptions of VO09, Z15, and L20. Lastly, in columns (14), (15), and (16), we report the Mg II-based M_{BH} estimates using each of the three Mg II velocity width parameters, FWHM, MAD, and σ_{line}, respectively. For our Mg II-based M_{BH} estimates, values are provided with and without the C IV EW term.

3.4. Mg II Covered by Both SDSS and GNIRS Spectra

For 53 sources from the GNIRS-DQS catalog of Paper I, in the $2.10 \lesssim z \lesssim 2.40$ redshift range, we have measurable Mg II profiles from both GNIRS and SDSS spectra. In order to confirm consistency across the SDSS and GNIRS spectra, we compare the effects of measuring these spectra in different epochs using different instruments by evaluating the differences in Mg II-based M_{BH} estimates stemming from each spectrum. For consistency, we used the VO09 method for calculating the Mg II-based M_{BH} estimates for all measurements in our comparison. This comparison is presented in Figure 9. The primary source of the systematic offsets in Figure 9 stems from the larger uncertainties of the Mg II emission-line measurements in the GNIRS spectra (see Paper I). Overall, we conclude that the two sets of measurements are

consistent with each other, and the mean offset between the $\log(M_{BH})$ values is only -0.012.

4. Discussion

In this work, we perform calibrations between C IV- and Mg II-based M_{BH} estimates and those based on the Hβ line using the largest, homogeneous sample of luminous quasars at high redshift that cover these three emission lines. The Hβ-based M_{BH} estimates that we calibrate to are accretion rate corrected according to the scaling relation presented in Du & Wang (2019) that involves the optical Fe II emission. We show that the inclusion of the C IV EW in our calibrations to these Hβ-based M_{BH} values allow for an additional accretion-rate correction in UV-based M_{BH} estimates (see also Paper I and Paper III). The inclusion of this term in our prescriptions leads to UV-based M_{BH} estimates that are closest to those obtained from Hβ.

Our results display improvements with respect to similar M_{BH} calibrations from previous studies that excluded such accretion-rate corrections. When utilizing σ_{line} as the velocity width parameter, we obtain the most robust prescription (Equation (11)) for C IV-based M_{BH} values, compared with previous studies of this kind. As shown in the bottom panel of Figure 2 we reduce the scatter of C IV-based M_{BH} estimates with respect to those from Hβ by $\sim$24%, $\sim$3%, and $\sim$33%

Table 2
Regression Coefficients

Emission Line	FWHM	MAD	σ_{line}
C IV (a, b)	$(5.172 \pm 0.196, 0.960 \pm 0.138)$	$(6.727 \pm 0.187, 0.250 \pm 0.131)$	$\mathbf{(6.299 \pm 0.169, 0.385 \pm 0.119)}$
Mg II only (c, d)	$\mathbf{(7.000 \pm 0.022, 0)}$	$(7.562 \pm 0.028, 0)$	$(7.309 \pm 0.031, 0)$
Mg II & C IV (c, d)	$\mathbf{(6.793 \pm 0.047, 0.005 \pm 0.001)}$	$(7.410 \pm 0.0068, 0.005 \pm 0.002)$	$(7.168 \pm 0.074, 0.004 \pm 0.002)$

Note. Resulting regression coefficients from Equations (6) and (7) for each of our velocity width parameters. Bold-faced coefficients are the recommended prescription for each emission line (see Section 4).

compared to the prescriptions of VP06, P17, and C17, respectively (see Figure 7). Similarly, the Pearson correlation coefficient between C IV-based and Hβ-based M_{BH} values improves from 0.09, 0.30, and 0.17 to 0.37, respectively. The slope of the best-fit relation between C IV-based and Hβ-based M_{BH} values also improves from 0.11, 0.28, and 0.25 to 0.36, respectively.

We also present a prescription (Equation (15)) for obtaining Mg II-based M_{BH} estimates when only the Mg II line is covered in the spectrum. This prescription is consistent with the findings of L20, confirming their results. It is interesting to note that in the high-redshift bin ($3.20 \lesssim z \lesssim 3.50$), the smallest scatter in the Mg II-based masses (when only the Mg II line is used) is obtained when the MAD is used as the velocity width. This scatter, $\sigma = 0.27$, is even smaller than the smallest scatter obtained for the entire sample of 225 sources (i.e., when the FWHM is used as the velocity width parameter) by $\sim 20\%$ (see upper panels of Figures 5 and 6). A larger sample of sources in this redshift range is necessary in order to draw firm conclusions as to whether a larger improvement can be achieved.

When we introduce the additional accretion-rate correction factor, in the form of the EW of C IV, we obtain a significantly improved Mg II-based M_{BH} value using Equation (16). Compared to the Mg II-based M_{BH} estimates derived from Equation (15), this prescription reduces the scatter in the calibration with Hβ-based M_{BH} estimates, by $\sim 15\%$. Similarly, the Pearson correlation coefficient is increased by $\sim 51\%$ (see Figure 6). As we find for the case when only the Mg II line is available, the scatter in the Mg II-based masses for the 23 sources in the highest-redshift range ($3.20 \lesssim z \lesssim 3.50$) is smaller by $\sim 20\%$ than that for the entire sample of 160 sources (see the bottom left panels of Figures 5 and 6), emphasizing the need for a larger sample in this redshift range. With respect to previous studies discussed throughout this work, our prescriptions, by design, correct the mean offset between UV-based and accretion-rate-corrected Hβ-based M_{BH} estimates. These corrections are critical, as manifested in Figures 7 and 8, where mean offsets of up to 0.40 and 0.14 appear in the μ values for C IV and Mg II, respectively.

We note that SE M_{BH} estimates, in general, have a 0.5-0.6 dex relative uncertainty and 0.7 dex absolute uncertainty (e.g., Table 5, VP06). Meanwhile, M_{BH} measurements that stem from RM campaigns have an inherent uncertainty of 0.3–0.5 dex due to their calibration against the M–$\sigma_\star$ relation (e.g., Peterson 2010; Vestergaard et al. 2011; Shen 2013; Ho & Kim 2014), and such observations are quite challenging at high redshift (e.g., Kaspi et al. 2021). While not being able to completely bridge the gap between these two approaches, the improvements this work provides to the accuracy and precision of SE UV-based M_{BH} estimates are considerable. We find that even when significant outliers are removed from all the M_{BH}

comparisons performed above, the resulting improvements in the scatter of up to $\sim 7\%$ do not warrant the removal of otherwise ordinary-looking sources from the sample. Overall, our work shows that when using a large, uniform calibration sample of quasars having coverage of C IV, Mg II, Fe II, and Hβ and when accounting for accretion rate both in the optical ($\mathcal{R}_{\text{Fe}}$) and in the UV (EW(C IV)), one can obtain the most reliable prescriptions for obtaining SE UV-based M_{BH} estimates.

4.1. Hα-based M_{BH} Values

The GNIRS-DQS spectral inventory of Paper I also provides measurements for the Hα emission line where available. In order to test the applicability of using this emission line as an M_{BH} indicator (e.g., Greene & Ho 2005), we ran the entire regression analyses presented in this work substituting FWHM (Hα) for FWHM(Hβ). The standard deviation, mean, and median of the difference between the $\log(M_{\text{BH}})$ estimates stemming from these two emission lines were 0.149, 0.114, and 0.105, respectively. We therefore conclude that the results based on Hα are roughly consistent with those obtained from Hβ, thereby confirming the applicability of using Hα to estimate M_{BH} values in quasars.
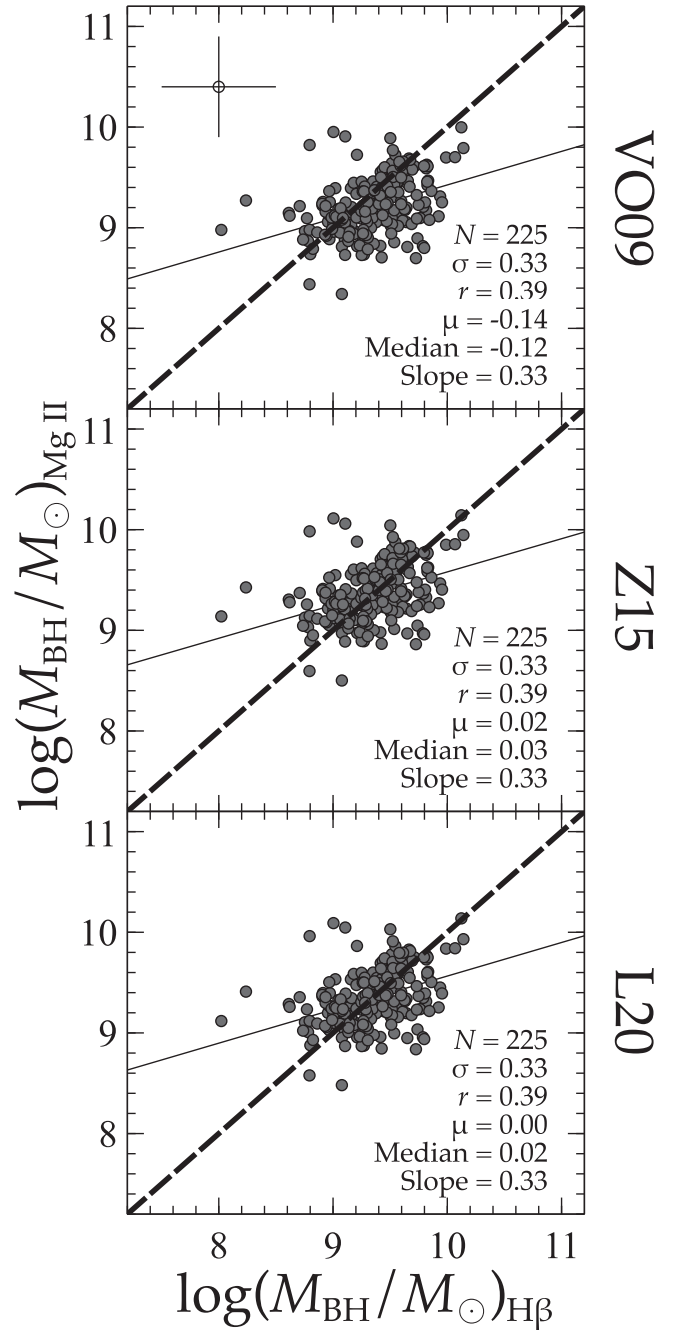
5. Conclusions

We provide prescriptions for reliable rest-frame UV-based M_{BH} estimates with respect to M_{BH} estimates obtained from the Hβ line. Utilizing the GNIRS-DQS catalog (Paper I), we calibrate SE C IV- and Mg II-based M_{BH} estimates to Hβ-based M_{BH} estimates using a linear-regression analysis that includes two basic accretion-rate observable indicators: the relative strength of the optical Fe II emission with respect to Hβ and the EW of the C IV emission line. We also investigate the use of different velocity width parameters for the C IV- and Mg II-based M_{BH} estimates and compare our results with previous studies. We summarize our main results as follows:

1. The Hβ-based M_{BH} estimates in this work are over-estimated by a factor of ~ 2 when the relative strength of the optical Fe II emission is not taken into account, consistent with the results of Maithil et al. (2022). All of the M_{BH} prescriptions throughout this work take that correction into account.
2. The inclusion of the C IV EW in our prescriptions considerably improves the precision of UV-based M_{BH} estimates. With respect to previous studies, our most reliable UV-based M_{BH} values reduce the scatter by $\sim 15\%$ when compared to Hβ-based values.
3. The preferred velocity width parameters for estimating M_{BH} using C IV and Mg II are σ_{line} and FWHM, respectively.
4. Equation (11) presents the prescription for obtaining the most reliable C IV-based M_{BH} estimates in the absence of
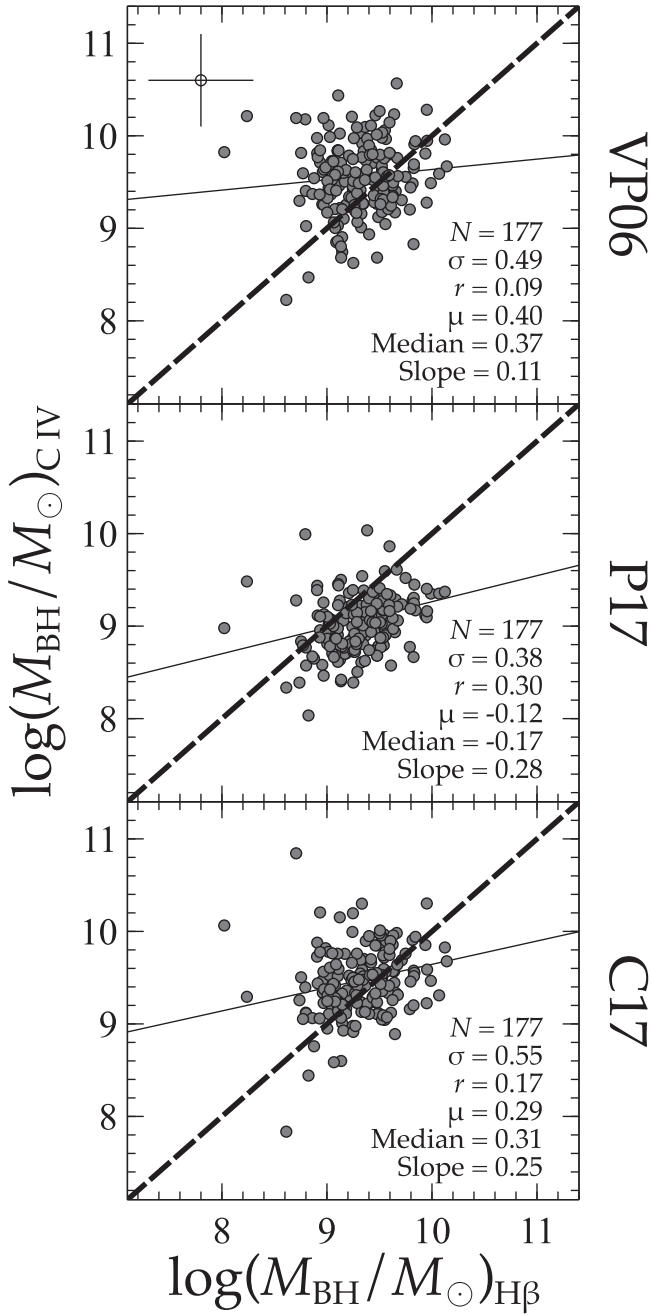
Figure 7. C IV-based M_{BH} estimates of our sample derived through the methodology of, from top to bottom: VP06, P17, and C17 against the Hβ-based M_{BH} estimates. The dashed lines represent one-to-one relationships, and the thin solid lines represent the best linear fit to the data in each panel. The most precise C IV-based M_{BH} values from this work were derived utilizing σ_{line} as the velocity width parameter (see the bottom panel of Figure 2). Our prescription shows a considerable improvement in the value of the Pearson correlation coefficient, r, albeit a modest improvement in the standard deviation, with respect to previous work. Additionally, our prescription corrects the mean offset (the μ value in each panel) due to considering the accretion rate when estimating Hβ-based M_{BH} values. Typical uncertainty of 0.5 dex on the M_{BH} values is displayed in the top panel for reference.

Figure 8. Mg II-based M_{BH} estimates of our sample derived through the methodology of, from top to bottom, VO09, Z15, and L20 against the Hβ-based M_{BH} estimates. The panels include all Mg II measurements available in SDSS and/or GNIRS. The dashed line in each panel represents a one-to-one relationship, and the thin solid line in each panel represents the best linear fit to the data. We find that our results are consistent with those of previous work when only measuring Mg II but are clearly improved with the inclusion of the C IV EW term (see the leftmost panels of Figure 6). Our prescriptions, by design, correct the mean offsets (the μ value in each panel) between the Mg II- and Hβ-based M_{BH} values with or without the inclusion of the C IV EW. Typical uncertainty of 0.5 dex on the M_{BH} values is displayed in the top panel for reference.

Mg II coverage. Conversely, if the source's spectrum only covers the Mg II line, the prescription from Equation (15) is preferred. Otherwise, Equation (16) presents the most robust prescription for UV-based M_{BH} estimates when there is spectral coverage of both C IV and Mg II emission lines.

5. NIR observations of additional sources at $3.20 \lesssim z \lesssim 3.50$ would allow us to test if further significant improvements can be achieved for UV-based M_{BH} estimates. Primarily, this redshift range reduces the uncertainty introduced

Table 3
M_{BH} Estimates

Quasar	Hβ			C IV						Mg II					
	FWHM	MAD	σ_{line}	VP06	P17	C17	FWHM	MAD	σ_{line}	VO09	Z15	L20	FWHM[a]	MAD[a]	σ_{line}[a]
(1)	(2)	(3)	(4)	(5)	(6)	(7)	(8)	(9)	(10)	(11)	(12)	(13)	(14)	(15)	(16)
SDSS J001018.88+280932.5	9.15	8.58	8.82	8.74	8.77	9.01	8.90	9.10	9.20	⋯	⋯	⋯	⋯ ⋯	⋯ ⋯	⋯ ⋯
SDSS J001249.89+285552.6	9.42	8.75	8.99	⋯	⋯	⋯	⋯	⋯	⋯	9.55	9.71	9.69	⋯ 9.69	⋯ 9.69	⋯ 9.70
SDSS J001355.10-012304.0	9.92	9.22	9.44	⋯	⋯	⋯	⋯	⋯	⋯	9.11	9.27	9.25	⋯ 9.25	⋯ 9.11	⋯ 9.07
SDSS J001453.20+091217.6	9.64	8.70	8.90	9.55	9.28	9.44	9.51	9.47	9.63	v9.05	9.22	9.20	9.20 9.20	9.36 9.33	9.33 9.30
SDSS J001813.30+361058.6	9.44	8.61	8.82	9.71	9.10	9.29	9.49	9.50	9.41	9.57	9.73	9.71	9.65 9.71	9.87 9.91	9.89 9.92
SDSS J001914.46+155555.9	9.32	8.81	9.08	9.30	8.83	9.38	9.32	9.20	9.22	9.37	9.53	9.51	9.54 9.51	9.27 9.22	9.22 9.17
SDSS J002634.46+274015.5	9.48	8.86	9.09	9.26	9.33	9.48	9.75	9.97	9.88	9.10	9.26	9.24	9.76 9.24	9.75 9.29	9.74 9.30
SDSS J003001.11-015743.5	9.18	8.50	8.71	9.25	8.70	9.17	9.36	9.17	9.07	⋯	⋯	⋯	⋯ ⋯	⋯ ⋯	⋯ ⋯
SDSS J003416.61+002241.1	9.33	8.71	8.96	9.16	8.61	9.13	9.00	8.91	8.90	9.27	9.44	9.41	9.36 9.41	9.21 9.23	9.18 9.20
SDSS J003853.15+333044.3	9.37	8.60	8.83	9.73	8.90	9.90	9.27	8.97	9.07	⋯	⋯	⋯	⋯ ⋯	⋯ ⋯	⋯ ⋯

Note.
[a] $\log(M_{BH}/M_\odot)$ estimates derived with (top row) and without (bottom row) the inclusion of the C IV EW, where available.

Data for 10 sources are shown.
(This table is available in its entirety in machine-readable form.)
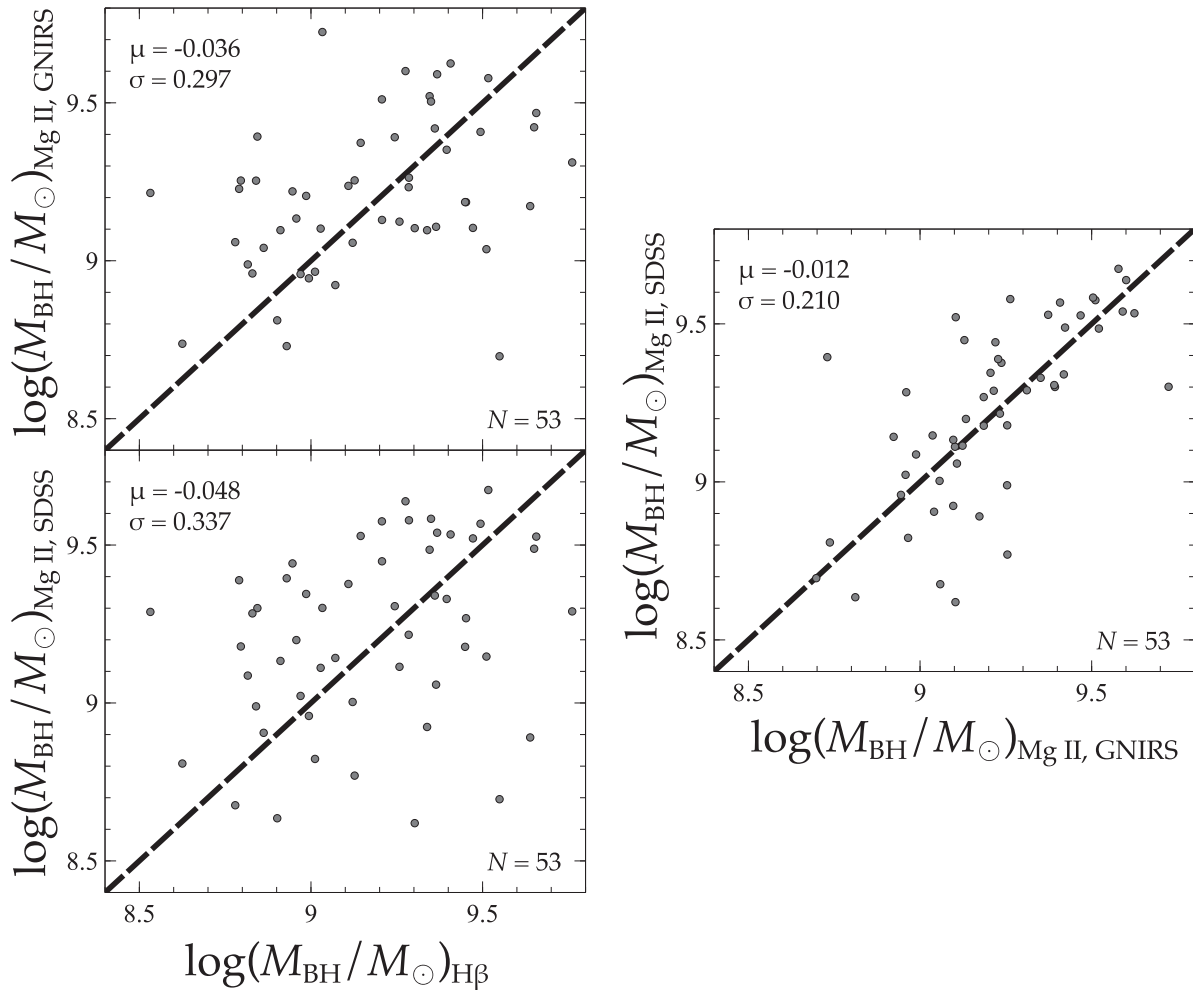
Figure 9. The upper leftmost and lower leftmost panels compare the GNIRS-DQS and SDSS, respectively, to the Mg II-based M_{BH} estimates based on the VO09 methodology against the Hβ-based masses. The rightmost panel presents the direct comparison of the SDSS- and GNIRS-DQS-based estimates to each other. In each panel, the mean (μ) and standard deviation (σ) of the residuals with respect to the one-to-one relationship (dashed line) are marked. Overall, we find that the measurements of the Mg II lines from the GNIRS spectra are consistent with the respective measurements from SDSS.

when measuring Mg II by shifting the emission line redward from the J band. A larger sample with high-quality spectral data at this redshift range may reveal further discrepancies between low- and high-luminosity objects.

In the coming decade, we expect that millions of high-redshift ($z \gtrsim 0.8$) quasars will have M_{BH} estimates derived from rest-frame UV emission lines through large spectroscopic surveys, e.g., the Dark Energy Spectroscopic Instrument (DESI; Levi et al. 2013; DESI Collaboration et al. 2016) and the 4 m Multi-Object Spectroscopic Telescope (de Jong et al. 2012). It is therefore crucial to derive the most reliable M_{BH} estimates for future high-redshift quasar catalogs using the prescriptions provided in this work.

ORCID iDs

Cooper Dix ● https://orcid.org/0000-0003-0192-1840
Brandon Matthews ● https://orcid.org/0000-0001-8406-4084
Ohad Shemmer ● https://orcid.org/0000-0003-4327-1460
Michael S. Brotherton ● https://orcid.org/0000-0002-1207-0909
W. N. Brandt ● https://orcid.org/0000-0002-0167-2453
Gabriel A. Ferrero ● https://orcid.org/0000-0001-9623-6218
Richard Green ● https://orcid.org/0000-0003-1245-5232
Paulina Lira ● https://orcid.org/0000-0003-1523-9164
Richard M. Plotkin ● https://orcid.org/0000-0002-7092-0326
Gordon T. Richards ● https://orcid.org/0000-0002-1061-1804
Donald P. Schneider ● https://orcid.org/0000-0001-7240-7449

References

Assef, R. J., Denney, K. D., Kochanek, C. S., et al. 2011, ApJ, 742, 93

Bao, D.-W., Brotherton, M. S., Du, P., et al. 2022, ApJS, 262, 14
Barth, A. J., Bennert, V. N., Canalizo, G., et al. 2015, ApJS, 217, 26
Baskin, A., & Laor, A. 2004, MNRAS, 350, L31
Baskin, A., & Laor, A. 2005, MNRAS, 356, 1029
Bentz, M. C., Denney, K. D., Grier, C. J., et al. 2013, ApJ, 767, 149
Bentz, M. C., & Katz, S. 2015, PASP, 127, 67
Bentz, M. C., Peterson, B. M., Netzer, H., Pogge, R. W., & Vestergaard, M.
    2009, ApJ, 697, 160
Blandford, R. D., & McKee, C. F. 1982, ApJ, 255, 419
Boroson, T. A., & Green, R. F. 1992, ApJS, 80, 109
Bromm, V., & Yoshida, N. 2011, ARA&A, 49, 373
Brotherton, M. S., Runnoe, J. C., Shang, Z., & DiPompeo, M. A. 2015,
    MNRAS, 451, 1290
Cackett, E. M., Gültekin, K., Bentz, M. C., et al. 2015, ApJ, 810, 86
Carniani, S., Maiolino, R., Marconi, A., et al. 2018, in AGN13: Beauty and the
    Beast (Zenodo), 68, https://indico.ict.inaf.it/event/524/overview
Chen, Z., Faber, S. M., Koo, D. C., et al. 2020, ApJ, 897, 102
Coatman, L., Hewett, P. C., Banerji, M., et al. 2017, MNRAS, 465, 2120
Dalla Bontà, E., Peterson, B. M., Bentz, M. C., et al. 2020, ApJ, 903, 112
de Jong, R. S., Bellido-Tirado, O., Chiappini, C., et al. 2012, Proc. SPIE, 8446,
    84460T
De Rosa, G., Decarli, R., Walter, F., et al. 2011, ApJ, 739, 56
Denney, K. D., Horne, K., Shen, Y., et al. 2016, ApJS, 224, 14
Di Matteo, T., Colberg, J., Springel, V., Hernquist, L., & Sijacki, D. 2008, ApJ,
    676, 33
Dix, C., Shemmer, O., Brotherton, M. S., et al. 2020, ApJ, 893, 14
Du, P., & Wang, J.-M. 2019, ApJ, 886, 42
Du, P., Zhang, Z.-X., Wang, K., et al. 2018, ApJ, 856, 6
DESI Collaboration, Aghamousa, A., Aguilar, J., et al. 2016, arXiv:1611.
    00036
Elias, J. H., Joyce, R. R., Liang, M., et al. 2006, Proc. SPIE, 6269, 62694C
Ferrarese, L., & Merritt, D. 2000, ApJL, 539, L9
Fonseca Alvarez, G., Trump, J. R., Homayouni, Y., et al. 2020, ApJ, 899, 73
Gebhardt, K., Bender, R., Bower, G., et al. 2000, ApJL, 539, L13
Greene, J. E., & Ho, L. C. 2005, ApJ, 630, 122
Greene, J. E., Peng, C. Y., Kim, M., et al. 2010, ApJ, 721, 26
Grier, C. J., Shen, Y., Horne, K., et al. 2019, ApJ, 887, 38
Grier, C. J., Trump, J. R., Shen, Y., et al. 2017, ApJ, 851, 21
Gültekin, K., Richstone, D. O., Gebhardt, K., et al. 2009, ApJ, 698, 198
GRAVITY Collaboration, Abuter, R., Aimar, N., et al. 2022, A&A, 657, L12
Ha, T., Dix, C., Matthews, B. M., et al. 2023, ApJ, in press (arXiv:2304.04783)
Ho, L. C., & Kim, M. 2014, ApJ, 789, 17
Homayouni, Y., Trump, J. R., Grier, C. J., et al. 2020, ApJ, 901, 55
Hoormann, J. K., Martini, P., Davis, T. M., et al. 2019, MNRAS, 487, 3650
Hopkins, P. F., Robertson, B., Krause, E., Hernquist, L., & Cox, T. J. 2006,
    ApJ, 652, 107
Hu, C., Li, S.-S., Yang, S., et al. 2021, ApJS, 253, 20
Kaspi, S., Brandt, W. N., Maoz, D., et al. 2021, ApJ, 915, 129
Kaspi, S., Maoz, D., Netzer, H., et al. 2005, ApJ, 629, 61
Kaspi, S., Smith, P. S., Netzer, H., et al. 2000, ApJ, 533, 631
Kellermann, K. I., Sramek, R., Schmidt, M., Shaffer, D. B., & Green, R. 1989,
    AJ, 98, 1195
Kelly, B. C. 2007, ApJ, 665, 1489
Kelly, B. C., & Merloni, A. 2012, AdAst, 2012, 970858
Kelly, B. C., Vestergaard, M., Fan, X., et al. 2010, ApJ, 719, 1315
Laor, A. 1998, ApJL, 505, L83

Le, H. A. N., Woo, J.-H., & Xue, Y. 2020, ApJ, 901, 35
Levi, M., Bebek, C., Beers, T., et al. 2013, arXiv:1308.0847
Lira, P., Kaspi, S., Netzer, H., et al. 2018, ApJ, 865, 56
Lyke, B. W., Higley, A. N., McLane, J. N., et al. 2020, ApJS, 250, 8
Maithil, J., Brotherton, M. S., Shemmer, O., et al. 2022, MNRAS,
    515, 491
Matthews, B. M., Dix, C., Shemmer, O., et al. 2023, ApJ, in press (arXiv:2304.
    09964)
Matthews, B. M., Shemmer, O., Dix, C., et al. 2021, ApJS, 252, 15
McLure, R. J., & Dunlop, J. S. 2004, MNRAS, 352, 1390
Mejía-Restrepo, J. E., Lira, P., Netzer, H., Trakhtenbrot, B., &
    Capellupo, D. M. 2018, NatAs, 2, 63
Onken, C. A., Ferrarese, L., Merritt, D., et al. 2004, ApJ, 615, 645
Onoue, M., Bañados, E., Mazzucchelli, C., et al. 2020, ApJ, 898, 105
Pancoast, A., Brewer, B. J., Treu, T., et al. 2014, MNRAS, 445, 3073
Park, D., Barth, A. J., Woo, J.-H., et al. 2017, ApJ, 839, 93
Peterson, B. M. 1993, PASP, 105, 247
Peterson, B. M., Somerville, R. S., & Storchi-Bergmann, T. 2010, in IAU
    Symp. 267, Co-Evolution of Central Black Holes and Galaxies (Cambridge:
    Cambridge Univ. Press), 151
Peterson, B. M., & Wandel, A. 1999, ApJL, 521, L95
Rakshit, S., Stalin, C. S., & Kotilainen, J. 2020, ApJS, 249, 17
Richstone, D. O., & Schmidt, M. 1980, ApJ, 235, 361
Runnoe, J. C., Brotherton, M. S., Shang, Z., & DiPompeo, M. A. 2013,
    MNRAS, 434, 848
Schindler, J.-T., Farina, E. P., Bañados, E., et al. 2020, ApJ, 905, 51
Shemmer, O., & Lieber, S. 2015, ApJ, 805, 124
Shen, Y. 2013, BASI, 41, 61
Shen, Y., Brandt, W. N., Dawson, K. S., et al. 2015, ApJS, 216, 4
Shen, Y., Brandt, W. N., Richards, G. T., et al. 2016, ApJ, 831, 7
Shen, Y., & Kelly, B. C. 2012, ApJ, 746, 169
Shen, Y., Richards, G. T., Strauss, M. A., et al. 2011, ApJS, 194, 45
Spergel, D. N., Bean, R., Doré, O., et al. 2007, ApJS, 170, 377
Suh, H., Civano, F., Trakhtenbrot, B., et al. 2020, ApJ, 889, 32
Sun, M., Xue, Y., Richards, G. T., et al. 2018, ApJ, 854, 128
The MathWorks Inc. 2018, MATLAB and Statistics Toolbox R2018b, Natick,
    Massachusetts, United States, MATLAB and Statistics ToolboxR2018b,
    Natick, Massachusetts, United States
Trakhtenbrot, B., & Netzer, H. 2012, MNRAS, 427, 3081
U, V., Barth, A. J., Vogler, H. A., et al. 2022, ApJ, 925, 52
Vanden Berk, D. E., Richards, G. T., Bauer, A., et al. 2001, AJ, 122, 549
Vestergaard, M., Denney, K., Fan, X., et al. 2011, in Narrow-Line Seyfert 1
    Galaxies and their Place in the Universe, vol. NLS1 (Trieste: PoS), 38
Vestergaard, M., & Osmer, P. S. 2009, ApJ, 699, 800
Vestergaard, M., & Peterson, B. M. 2006, ApJ, 641, 689
Vestergaard, M., & Wilkes, B. J. 2001, ApJS, 134, 1
Woo, J.-H., Le, H. A. N., Karouzos, M., et al. 2018, ApJ, 859, 138
Woo, J.-H., Yoon, Y., Park, S., Park, D., & Kim, S. C. 2015, ApJ, 801, 38
Wu, Q., & Shen, Y. 2022, ApJS, 263, 42
Yang, J., Wang, F., Fan, X., et al. 2021, ApJ, 923, 262
York, D. G., Adelman, J., Anderson, J. E., Jr., et al. 2000, AJ, 120, 1579
Yu, L.-M., Bian, W.-H., Wang, C., Zhao, B.-X., & Ge, X. 2019, MNRAS,
    488, 1519
Yu, L.-M., Zhao, B.-X., Bian, W.-H., Wang, C., & Ge, X. 2020, MNRAS,
    491, 5881
Zuo, W., Wu, X.-B., Fan, X., et al. 2015, ApJ, 799, 189